Supplementary Information

Dual-readout proximity hybridization-regulated and photothermal-amplified protein analysis based on MXene nanosheets

Huizhu Ren[a], Shupei Zhang[b], Yitian Huang[a], Yanjie Chen[a], Liang Lv[b] and Hong Dai*[a]

a College of Chemistry and Material, Fujian Normal University, Fuzhou, Fujian, 350108, China

b College of Chemical and Material Engineering, Quzhou University, Quzhou, Zhejiang, 32400, China.

Table of Contents:

1. Materials and Reagents

Human epididymis protein 4 (HE4) and mouse monoclonal anti-HE4 antibodies (Ab_1 and Ab_2) were purchased from Protein Tech Group, Inc. (Wuhan, China). Prostate specific antigen (PSA) and interleukin-6 (IL-6) were supplied by Linc-Bio Science Co., Ltd. (Shanghai, China). Thyroglobulin (TG) was bought from Mercak Biotechnology Co. Ltd. (Wuhan, China). Bovine serum albumin (BSA) was obtained from Biss Inc. (Beijing, China). Human serum samples were kindly provided by Fujian Provincial Maternity and Children′s Hospital (Fuzhou, China). Polyethylenimine (PEI) and thionin acetate salt were purchased from Aladdin Reagent Co., Ltd. (Shanghai, China). Sulfosuccinimidyl-4-(N-maleimidomethyl) cyclohexane-1-carboxylate (SMCC), Dithiothreitol (DTT), 6-mercapto-1-hexanol (MCH) and tris-(2-carboxyethyl) phosphine hydrochloride (TCEP) were obtained from Aladdin Bio-Chem Technology Co., Ltd (Shanghai, China). 0.1 M phosphate buffered saline (PBS) at several pH values were consisted of 0.1 M NaH_2PO_4, 0.1 M Na_2HPO_4 and 0.1 M KCl. All oligonucleotides were synthesized and HPLC-purified by Sangon Biotechnology Inc. (Shanghai, China) as shown in Table S1. Aluminum titanium carbide (Ti_3AlC_2) was purchased from Forsman Technology Co., Ltd. (Beijing, China). All the other reagents were of analytical grade and without further purification.

Table S1. Sequences of all the oligonucleotides used in this work.

Oligonucleotide	Sequence (5'-3')
DNA_1	5'-**GCT GAG GTT** AT***C AAG AC***T TTT TTT ATC ACA TCA GGC TCT AGC GTA TGC TAT TG-SH-3′
DNA_2	5'-SH-TAC GTC CAG AAC TTT ACC AAA CCA CAC CCT TTT TTT ***GTC TTG*** GCT GAG GAT-3
Capture DNA_3	5'-ATC CTC AGC **AAC CTC AGC** AGC G-SH-3′ ,
Ref DNA_4	5'-TTG GTA AAG TTC TGG ACG TAT CTC CCA TTG TAG TAT CTT GTA GTA TCT CCC ATC ACC AGT CAA TAG CAT ACG CTA GAG CC-3′

The binding regions between capture DNA_3 and DNA_1 are shown in bold; the binding regions between capture DNA_3 and DNA_2 are shown in underlined; the bindings regions between DNA_1 and DNA_2 are shown in bold and italics, respectively.

2. Apparatus

All the electrochemical measurements were performed on a CHI 660E electrochemical workstation (CH Instruments, Inc, Shanghai, China) with the conventional three-electrode system composed of a glassy carbon electrode (GCE) as working electrode, a Pt wire as counter electrode, and Ag/AgCl as reference electrode. Scanning electron microscopy (SEM) was operated with Hitachi S-4800 scanning electron microscope and the transmission electron microscopy (TEM) image was taken by JEM-2100 transmission electron microscope. UV–vis absorption spectra were recorded on a UV 1900 spectrophotometer (Shanghai, China). Fourier transform

infrared spectroscopy (FTIR) was performed on a NICOLET 6700 (Thermo Fisher Scientific Inc., USA).

3. Preparation of the materials

3.1 Synthesis of PEI-TiO_2 NDs

TiO_2 NDs were synthetized according to the previous work [1]. Subsequently, 1 mL PEI aqueous solution (1 wt%) was added in 1 mL TiO_2 NDs dispersion solution (3 mg/mL), and the mixture was continuously stirred for 6 h at room temperature. Then the precipitate PEI-TiO_2 NDs were collected by centrifugation at 10,000 rpm for 10 min and wash with ultrapure water for three times to remove the redundant PEI. After drying, the product of PEI-TiO_2 NDs was redispersed in 1 mL ultrapure water for the subsequent use.

3.2 Preparation of MXene@Thi composite

MXene was prepared from bulk Ti_3AlC_2 through the HF etching process according to the previous report with minor modification.[2] Briefly, 1 g Ti_3AlC_2 powders were immersed in 20 mL of 40% HF under the magnetic stirring for 24 h at 45 °C. The reaction product was collected by centrifuging at 8000 rpm and washing with ultrapure water three times until the pH of suspension approached neutral. Finally, the resultant solid was dried at 80 °C overnight and the black powder of MXene nanosheet was prepared.

To obtain the functionalized MXene for the further modification, 5 mg as-prepared MXene nanosheet was dispersed in 1 mL ethanol, and then evenly mixed with 20 μL 3-aminopropyl triethoxysilane (APTES) under constantly stirring over

night at room temperature. The resulting modified MXene nanosheet was obtained after the centrifugation for 10 min and purified by multiple washing with ultrapure water, then dispersed and sonicated in 1 mL ultrapure water. 200 μL glutaraldehyde solution (2.5 wt %) was added into the prepared MXene nanosheet dispersion solution and stirred for 40 min. Subsequently, 1 mL Thi aqueous solution (5 mg/mL) was mixed with the above functionalized MXene nanosheet, and the mixture with stirring lasting for 5 h in the dark. Likewise, the resultant product of MXene@Thi composite was collected in the same procedures mentioned above, which was dispersed in 1 mL ultrapure water and then stored in the dark prior to use.

3.3 Preparation of DNA_1-Ab_1 and DNA_2-Ab_2 affinity probes

The affinity probes (DNA_1-Ab_1 and DNA_2-Ab_2) were prepared by chemically cross-linking according to the previous procedure.[3] Briefly, 200 μL Ab_1 or Ab_2 solution (0.2 mg/mL) was reacted with 50 μL of SMCC (0.4 mM) in 0.1 M PBS (pH 7.4) containing 0.15 M NaCl and 0.02 M EDTA for 2 h at room temperature. Meanwhile, 3 mL of 10 μM DNA_1 or DNA_2 was added into 4 mL of 10 μM DTT in PBS for 1h at 37 °C to reduce dimerization of DNA. The obtained Ab_1 or Ab_2 were mixed with reduced DNA_1 or DNA_2 to incubate over night at 4 °C, respectively. The resulted DNA-Ab affinity probes were purified by ultrafiltration for three times and re-dissolved in 100 μL PBS.

3.4 The treatment of serum samples

The treatment of serum samples was similar to the previous report.[4] The clinical serum samples were obtained from Fujian Provincial Maternity and Children Hospital.

Prior to use, the human serum was obtained by centrifugation at 4000 rpm for 5 min. All the samples were diluted 5-folds by 0.1 M phosphate buffer solution (pH 7.4) before measurements.

3.5 Fabrication and detection of the immunosensor

The bare GCE (3 mm diameter) was sequentially polished with Al_2O_3 powder of 0.3 μm and 0.05 μm, following the washed ultrasonically with the mixture of ethanol and ultrapure water, and finally drying at room temperature. 5 μL PEI-TiO_2 NDs dispersion solution (3 mg/mL) was dropped on GCE and dried in the air. The electrochemical deposition process was performed on modified PEI-TiO_2 NDs/GCE in 1 % $HAuCl_4$ solution at the potential of −0.2 V for 30 s, thus Au/PEI-TiO_2 NDs/GCE was obtained. 5 μL capture DNA_3 (10 μM) was immobilized onto the surface of above-modified electrode and incubated via Au-S bonding for 3 h at room temperature. After rinsing with 10 mM PBS, the resulting electrode was immersed into 100 μL of 1 mM MCH solution for 30 min to block the nonspecific adsorbed sites. The HE4 detection was performed by dropping 5 μL of mixture solution containing 10 μM DNA_1-Ab_1, 10 μM DNA_2-Ab_2 and different concentrations of HE4 standard solution onto the electrodes for 60 min at room temperature to facilitate DNA hybridization. After terminated by thoroughly washing, the electrode was immersed into 5 mg/mL MXene@Thi composite for 50 min and the residual composite was washed away from the electrode. Thus the resulting electrode was prepared for the follow-up electrochemical and temperature measurement.

4. Results and discussions

4.1 Characterizations

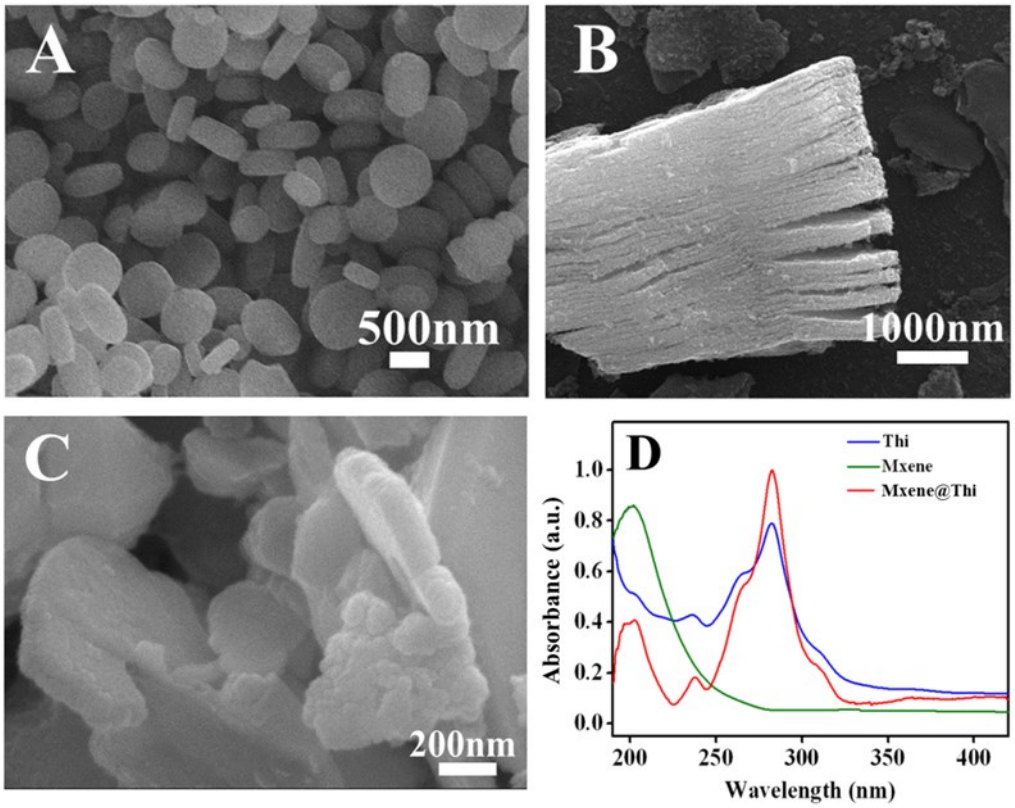

Fig. S1. SEM images of (A) TiO_2 NDs, (B) the original Ti_3AlC_2 and (C) Ti_3C_2-MXene after HF etching. (D) The UV–vis absorption of Mxene, Thi and Mxene@Thi.

SEM images were recorded to confirm the morphology and structure of as-prepared TiO_2 NDs and MXene. As displayed in Fig. S1A, TiO_2 showed the highly consistent diameters of about 500 nm and approximate-disc structure, demonstrating the large specific surface area were beneficial to fabricate sensing substrate. The morphology was identical with previous reports, thus TiO_2 NDs were successfully synthesized. Fig. S1B revealed Ti_3AlC_2 was bulk with the thickness of about 4 μm, while after the HF etching process, as clearly shown in Fig. S1C, the obtained MXene nanosheet exhibited single-layer morphology and the thickness reduced to 100 nm,

indicating the single layer MXene nanosheet was successfully exfoliated, and the layer structure was favorable for the immobilization of Thi to further construct the signal source container. As shown in Fig. S1D, the UV-vis absorption spectra provided additional evidence of the conjugation between MXene and Thi, a strong spectrum adsorption at 285 nm belong to the corresponding characteristic peak of Thi solution, while the MXene nanosheet exhibited adsorption peak located at 210 nm. For MXene@Thi composite, there were two wide absorption peaks at 210 nm and 285 nm, indicating the successful loading of Thi and truly existed on the MXene nanosheet.

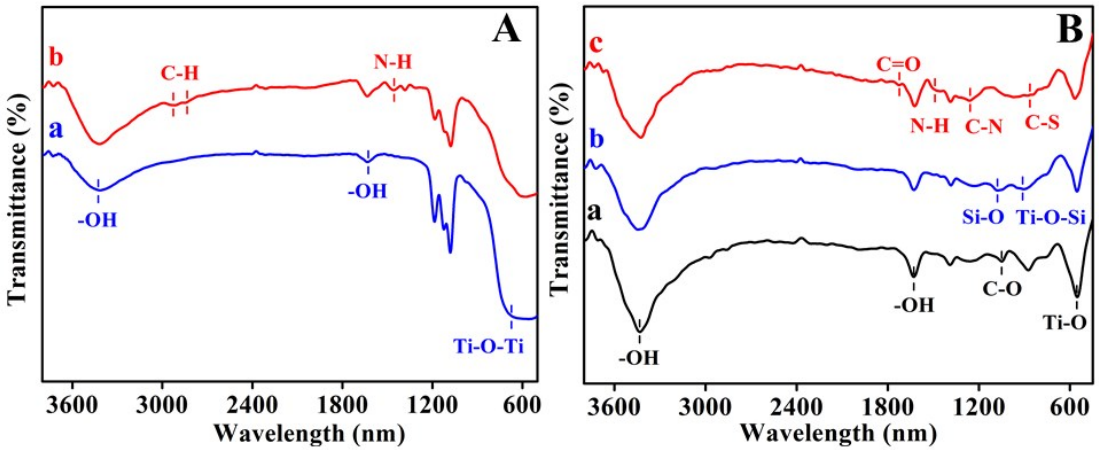

Fig. S2. The FTIR spectra of (A): (a) TiO_2 NDs and (b) PEI-TiO_2 NDs. (B): (a) MXene, (b) MXene-APTES and (c) MXene@Thi.

The FTIR has been considered as an effective method to analyze the preparation of the materials. As shown in **Fig. S2A**. For both original TiO_2 NDs (curve a) and PEI-TiO_2 NDs (curve b), the adsorption peaks at 3424 cm^{-1} and 1664 cm^{-1} were related to -OH group, and characteristic peaks observed below 640 cm^{-1} was assigned to TiO_2.[5] Typical peaks at 2946~2846 cm^{-1} were assigned to the C-H bond stretching

vibration in PEI. The presence of N−H bending (at 1642 cm^{-1}) proved PEI has been modified on the surface of TiO_2 NDs [6, 7]. Moreover, as the FTIR spectrum of pristine MXene showed in **Fig. S2B** (curve a), the sharp peaks around 3432 cm^{-1} and 1628 cm^{-1} were attributed to -OH, indicating the high hydrophilic property of MXene. The peak at 1049 cm^{-1} and 553 cm^{-1} were assigned to C-O and Ti-O bond, respectively. After the modification of APTES, the additional peaks of Si-O (at 1076 cm^{-1}) and Si-O-Ti (910 cm^{-1}) appeared in MXene-APTES (curve b), suggesting the efficient grafting of amino-terminal silanes onto MXene surface.[8] In the MXene@Thi composite (curve c), 1732 cm^{-1} was assigned to C=O of glutaraldehyde.[9] The characteristic peaks including the stretching vibration of N-H (1493 cm^{-1}), C-N (1266 cm^{-1}), and the bending vibration of C-S (903 cm^{-1}) were assigned to Thi.[10] These results demonstrated the successful preparation of MXene@Thi composite.

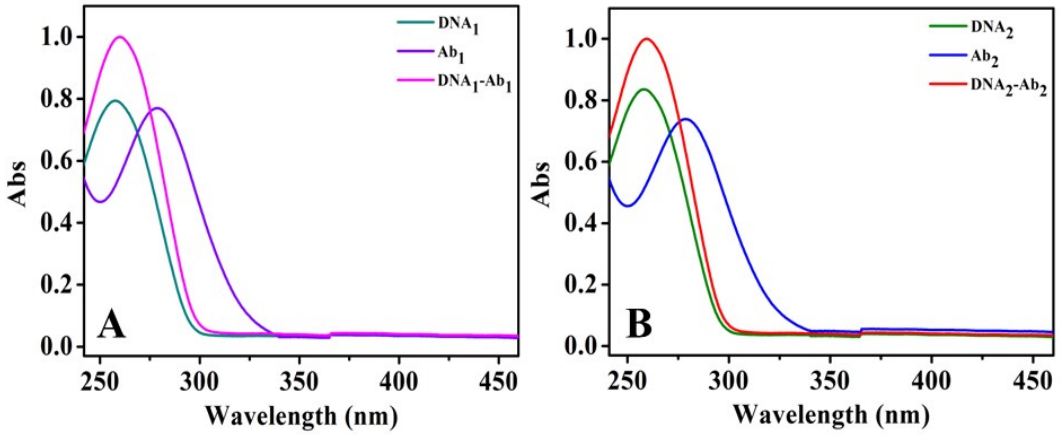

Fig. S3 The UV–vis absorption of (A) 10 μM DNA_1-Ab_1, 10 μM DNA_1 and 0.2 mg/mL Ab_1; (B) 10 μM DNA_2-Ab_2, 10 μM DNA_2 and 0.2 mg/mL Ab_2.

The synthesized DNA affinity probes (DNA_1-Ab_1 and DNA_2-Ab_2) were characterized through UV−vis spectroscopy and shown in Fig. S3. There were two

typical spectrum adsorptions at 260 nm and 280 nm, which were individually correspond to DNA and antibody. It was noted that DNA-Ab exhibited an integrated peak with a slight spectral red shift at about 262 nm, indicating the successful conjugation of DNA onto antibody.

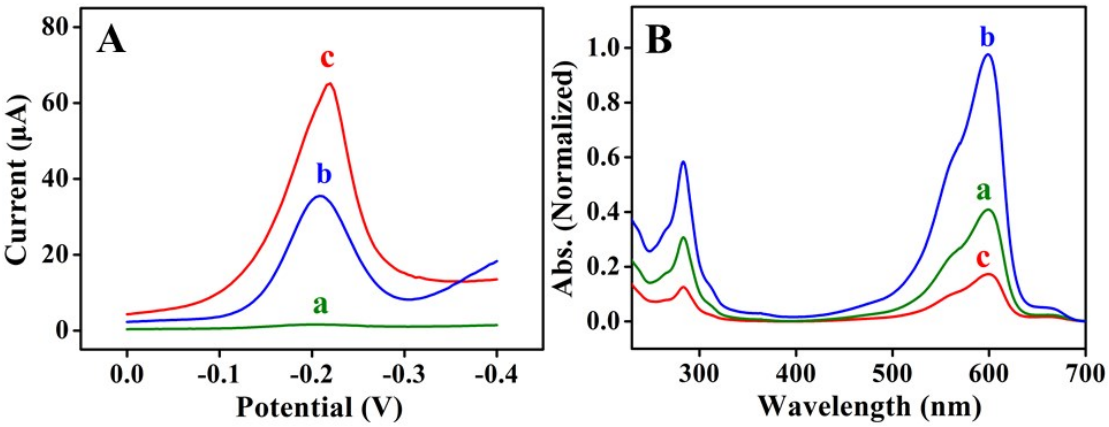

Fig. S4. (A) The SWV response of different modified electrode: (a) GO@Thi/GCE, (b) CNTs@Thi/GCE and (c) MXene@Thi/GCE. (B) The UV-vis spectrum after the saturated adsorption for Thi onto (a) GO, (b) CNTs and (c) MXene

It was said that low-dimensional materials have been regarded as ideal adsorbents toward organic dyes due to the large surface areas. Among them, carbon-based nanomaterials such as graphene oxide (GO) and carbon nanotubes (CNTs) have gained extensive research,[10, 11] which were compared with MXene to estimate the load capacity of Thi. In the comparative experiments, 500 μL of Thi solution (5 mM) was respectively added into 1 mL the above-mentioned nanomaterials, including GO, CNTs and MXene with the same concentration of 2 mg/mL to assess their adsorption properties. After the saturated adsorption, the collected precipitate was determined by SWV measurement, and the residual amount of Thi in supernatant was studied for the

subsequent UV-vis analysis. As shown in Fig. S4A, GO@Thi composite (curve a) exhibited a weak SWV response due to the poor conductivity of GO. In comparison, CNTs as the typical conductive carbon materials, whose signal intensity was stronger than that of GO (curve b). Notably, the most significant signal of MXene@Thi composite (curve c) was observed, which was contributed to the large surface area and excellent conductivity of MXene.[12, 13] Furthermore, the load capacity of different nanomaterials was further investigated by UV-vis absorption spectrum. As shown in Fig. S4B, it was obvious that MXene exhibited the outstanding adsorption capacity of Thi compared with GO and CNTs. These results were in accordance with the previous reports, because the hydrophilic surface such as -OH and -O groups on MXene were beneficial to adsorb cationic dyes than other adsorption structures.[14] Therefore, it was strongly suggested that MXene was suitable as the ideal container for the design of signal tags.

4.2 Calculation of the specific surface area

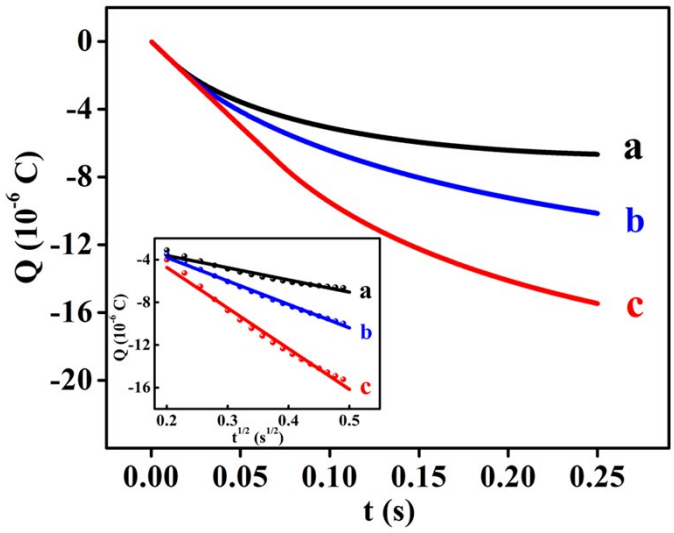

Fig. S5 Chronocoulometry of (a) GCE, (b) GO/GCE, (c) MXene/GCE in 5 mM $[Fe(CN)_6]^{3-/4-}$ containing 0.1 M KCl solution. The insert was the linear relationship between the charge (Q) and the square root of scan time ($t^{1/2}$).

The effective specific surface area of Mxene modified electrode was studied by chronocoulometry.[15] The charge on Mxene/GCE (Q) against the scan time (t) could be described by Anson equation,[16] thus the linear relationship between Q and square roots of t was established as followed:

$$Q(t) = \frac{2nFAcD^{1/2}t^{1/2}}{\pi^{1/2}} + Q_{ads} \quad (1)$$

Where n denotes the number of transferred electron (n = 1), A is effective specific surface area of working electrode, c is concentration of substrate (5.0×10^{-3} mol L^{-1}), D is diffusion coefficient (6.3×10^{-5} cm^2 s^{-1}), Q_{ads} is Faradic charge (3.0×10^{-6} C), F and π have their usual value. Accordingly, the apparent electroactive surface of MXene/GCE can be obtained by the slopes (κ) of the plot of Q versus $t^{1/2}$ and equation (1) may be simplified to:

$$A = \frac{\kappa\pi^{1/2}}{2nFcD^{1/2}} \quad (2)$$

As shown in **Fig. S5**, the slopes of a-c are respectively to -1.14×10^{-5}, -2.20×10^{-5} and -3.81×10^{-5}. The surface area of bare GCE (curve a) is 0.0033 cm^2, while, the effective specific surface area of GO/GCE and MXene/GCE can calculate to be 0.0064 cm^2 and 0.011 cm^2, respectively. The surface area of MXene/GCE was larger than that of bare GCE and GO/GCE, indicating MXene was a promising 2D layered material compared with the traditional GO due to the large surface area.

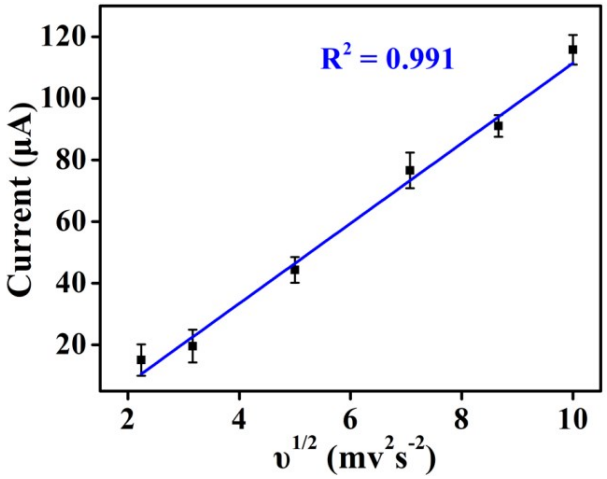

Fig. S6 The plot for the dependence of Mxene@Thi/GCE peak current on the square root of different scan rates: 5, 10, 25, 50, 75 and 100 mVs^{-1} in 0.1 M PBS (pH 7.4).

To gain insight into the mechanism of the temperature induced electrochemical signal amplification, the relationship between current intensity and scan rates for MXene@Thi/GCE was further investigated and the results are shown in Fig. S6(ESI†). Apparently, the peak current increased linearly with the square root of scan rate, which was in agreement with the Randles–Sevcik equation.[25] It was confirmed

that the electrochemical reaction of MXene@Thi on the sensing interface was a diffusion-controlled process. Under NIR light irradiation, MXene@Thi acted as the thermal converter to increase the electrode temperature by the photothermal effect, converting laser energy into heat to form the temperature gradient layer near the electrode surface. Therefore, the diffusion rate and convection of solution on the sensing interface were improved at the higher temperature, leading to the enhanced electrochemical signal.[26]

4.3 The feasibility of PHA

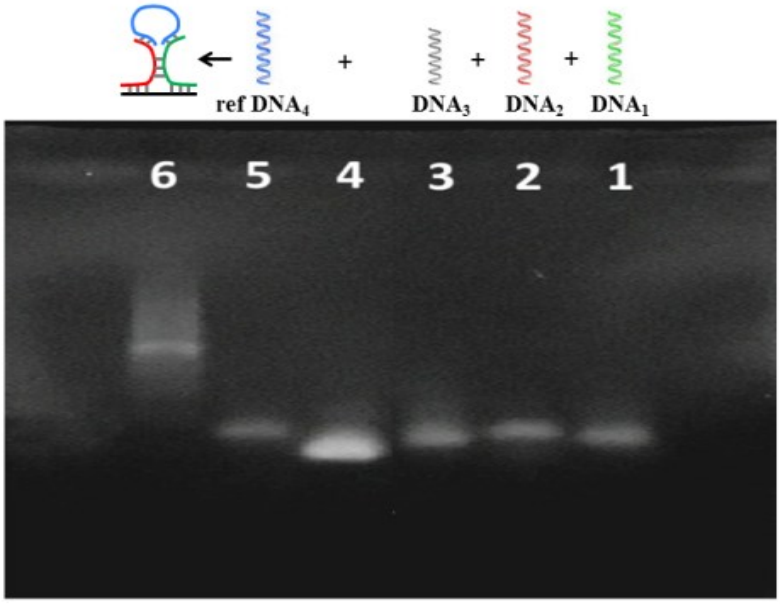

Fig. S7. AGE image of different DNAs: Lane 1, DNA_1; Lane 2, DNA_2; Lane 3, capture DNA_3; Lane 4, the mixture of capture DNA_3, DNA_1 and DNA_2; Lane 5, ref DNA_4; Lane 6, the mixture of capture DNA_3-DNA_1-ref DNA_4-DNA_2.

To further verify the feasibility of the target-triggered PHA, ref-DNA (see details in Table S1) was utilized to mimic the function of HE4 in the AGE analysis. As shown in Fig. S7, the single DNA_1, DNA_2, DNA_3 and ref DNA_4 kept the clear bands,

respectively (lane 1, 2, 3 and 5). Besides, the mixed bands were observed (lane 4) without new bands appeared, indicating there was no hybridization between DNA_1, DNA_2 and DNA_3. However, once adding the ref-DNA_4 into the complex DNA (DNA_1, DNA_2 and DNA_3), an obvious migration band was generated (lane 6), due to the successful formation of hybridized complex (DNA_3/DNA_1/ref-DNA/DNA_2) with the assistance of ref-DNA_4.

4.4 Optimized conditions

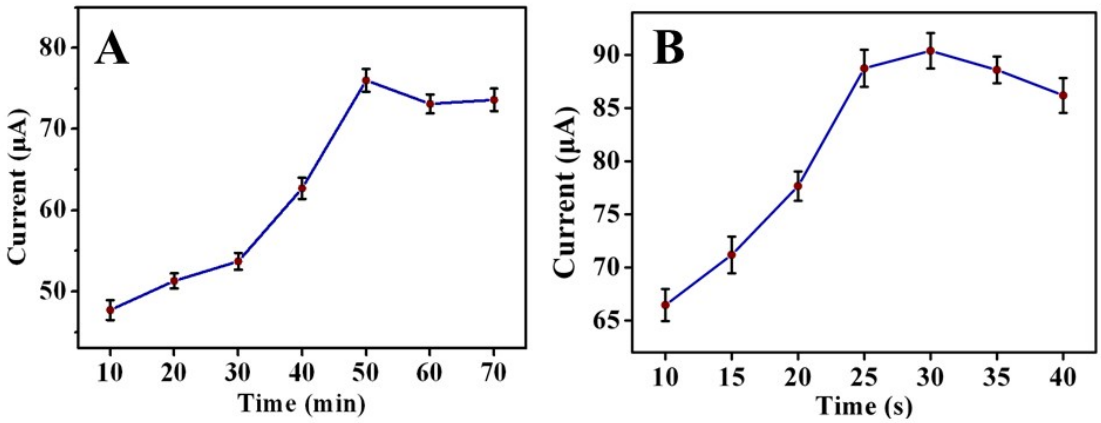

Fig. S8. (A) The SWV responses of TiO_2 NDs-PEI/GCE with different modified time in 0.1 M PBS (pH 7.4) containing 1 mg/mL thionine solution and (B) the immunosensor with different Au NPs electrodeposition time.

As shown in Fig. S8 (A), the signal response was increased with the modified time increasing of TiO_2 NDs-PEI electrode, and up to 50 min reached the balance, indicating that 50 min was suitable to the immobilization of substrate and was chosen for the further Au NPs electro-deposition step. Afterwards, different Au NPs electro-deposition times on electrode surface were optimized. As observed in Fig. S8 (B), the immunosensor signal gradually strengthened with the extension of electro-deposition

time, owing to the deposited Au NPs onto electrode surface effectively accelerated electron transfer, as well as provided the more active sites for capture DNA immobilization. Thus 30 min was the best Au NPs electro-deposition time for the further experiments.

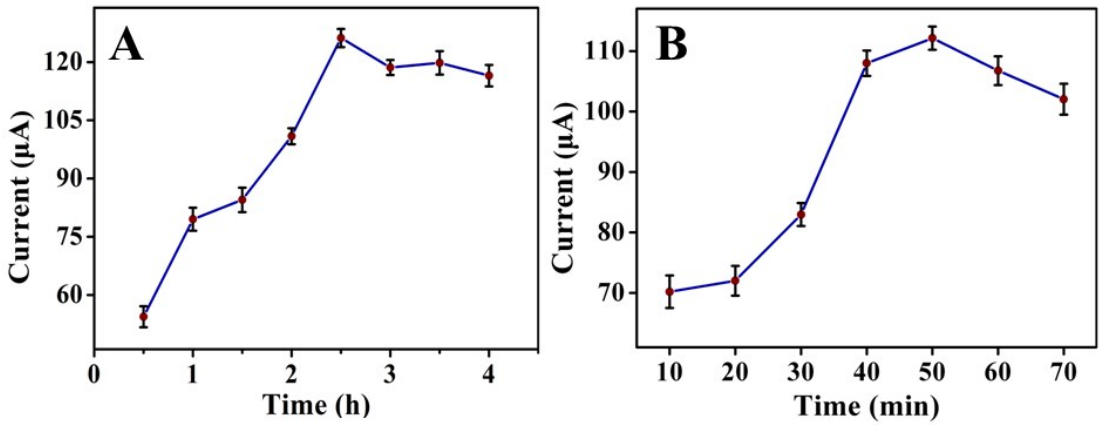

Fig. S9. (A) The SWV responses of the immunosensor with different immobilization time of capture DNA_3 and (B) the incubation time of 10 ng/mL HE4.

To obtain the higher signal and capacity of signal tag, the immobilization time of capture DNA_3 was a crucial factor and depicted in Fig. S9 (A), with the increase amount of capture DNA_3 immobilization the signal of immunosensor rapidly enhanced and then reached a plateau after about 2.5 h, thus the maximum immobilization quantity of capture DNA_3 was obtained, which was propitious to the subsequent ds-DNA generation. In order to optimize the incubation time of HE4, the target induced hybridization reaction between recognition probes was performed in different periods of time and investigated in Fig. S9 (B), the highest signal value was obtained when the incubation time of HE4 was 50 min, which indicated the maximum hybridization efficiency and the saturated capacity for signal tag intercalation.

Therefore, 50 min was chosen as the optimum incubation time throughout the experiments.

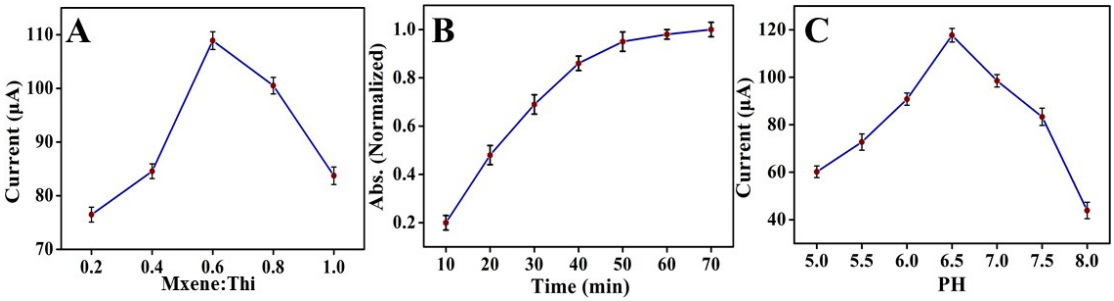

Fig. S10. (A) The SWV curves of different volume ratio between Mxene and Thi, (B) the immobilization time of Thi on MXene and (C) the pH effect.

The volume ratio optimization between Mxene and thionine was necessary to the immunosensor. As shown in Fig. S10 (A), when the volume ratio was 0.6 the signal reached the pinnacle, indicating that the maximum loading of Thi on the surface of Mxene nanosheet with the best intercalation efficiency, thus the volume radio of 0.6 was used in the experiments mentioned above. To optimize the most proper loading amount of Thi on MXene, different immobilization time of Thi was also investigated. As exhibited in Fig. S10 (B), the absorption intensity of Thi gradually increased with the immobilization time extended from 10 to 70 min, and reached the plateau at 50 min due to the saturated adsorption of Thi on MXene. Accordingly, 50 min was selected as optimal immobilization time for the subsequent measurements. Besides, pH 6.5 was chosen as the appropriate pH value of test solution in Fig. S10 (C).

Table S2. Recovery measurements of HE4 in human serum sample (n=3)

Sample	Added (ng/mL)	Electrochemical detected (ng/mL)	Recovery (%)	Temperature detected (ng/mL)	Recovery (%)
1	0	0.637	--	0.628	--
2	5	5.574, 5.203, 5.462	96.0	5.518,5.806, 5.842	101.6
3	0.1	0.711, 0.740, 0.706	97.6	0.749, 0.724, 0.762	102.3
4	0.01	0.668, 0.653, 0.647	101.4	0.625, 0.596, 0.573	93.7

Recovery = $(C_{detected} / C_{added}) \times 100\%$

Table S3. Comparison with various methods of the HE4 detection.

Detection methods	Detection range	LOD	Reference
ELISA	19.5 – 1250 ng/mL	19.5 ng/mL	[17]
Photoelectrochemical	0.1pg/mL–10ng/mL	0.03 pg/mL	[18]
Surface enhanced Raman spectroscopy	1 pg/mL–10 ng/mL	100 fg/mL	[19]
Localized surface plasmon resonance	10 – 10,000 pM	4.0 pM	[20]

Temperature	10^{-6}–10 ng/mL	3.3×10^{-7} ng/mL	This work
Electrochemical	10^{-6}–10 ng/mL	3.3×10^{-7} ng/mL	This work

Table S4. Comparison with other electrochemical methods for HE4 detection

Output mode	Detection range	LOD	Reference
Single-signal	1.0 ~ 100 ng/mL	0.2 ng/mL	[21]
Single-signal	10 fg ~ 100 ng/mL	3.4 fg/mL	[22]
Single-signal	0.001 ~ 50 ng/mL	0.487 pg/mL	[23]
Single-signal	0.002 ~ 20 ng/mL	1.5 pg/mL	[24]
Dual-signal	10^{-6} ~ 10 ng/mL	3.3×10^{-7} ng/mL	This work

Compared with this proposed dual-readout method, these reported electrochemical immunosensors only allow the single electrochemical signal readout. Besides, they rely on the traditional sandwich recognition format and common signal amplification strategy. In this work, the amplified electrochemical signal and temperature signal were dexterously achieved by photothermal effect. The obtained temperature signal was easily monitored by an ordinary thermometer, which exhibited the broad application prospect in POCT field. Therefore, this dual-readout immunoassay provided the more accurate result by the mutual calibration of these output signals. Moreover, taking the advantage of PHA, this one-step recognition process was simple and time-saving in homogeneous solution. In this study, PHA was utilized as a highly selective and more flexible assay for HE4 detection with the wider linear range and lower detection limit (**Table S4**).

Table S5 Determination of HE4 in serum samples using ELISA method and the dual-readout strategy in this work (n=3).

Method	ELISA		Electrochemical		Temperature	
Sample	Found (ng/mL)	RSD (%)	Found (ng/mL)	RSD (%)	Found (ng/mL)	RSD (%)
Positive (+)	4.153	1.88	4.147	2.46	4.128	3.87
Negative (-)	2.32×10^{-3}	2.93	2.11×10^{-3}	3.11	2.47×10^{-3}	3.25

In order to verify the practical application of this immunoassay, the standard addition method was employed for real sample analysis. Different concentrations of HE4, (5 ng mL^{-1}, 0.1 ng mL^{-1}, 0.01 ng mL^{-1}) were spiked into diluted serum samples, and the recoveries of HE4 were monitored by electrochemical and temperature determination. As shown in Table S2 (ESI†), the recovery rates of HE4 were calculated to be 96.0–101.4% using the electrochemical model, and the results by the temperature determination were in the range of 93.7–102.3%. In addition, the detection results for HE4 in serum samples using ELISA as reference method are shown in Table S5 (ESI†). The previous results suggested that this dual-readout immunoassay showed promise as a potential application to detect HE4 in clinical samples. The concentration of HE4 in patient serum samples (+) and healthy serum samples (-) were detected by the developed dual-readout method, the results were

shown in **Table S5.** Besides, the obtained detection results were also compared with commercial enzyme-linked immunosorbent assay (ELISA) kit. Obviously, the results exhibited good accordance with that calculated by ELISA method, suggesting the reliability of our proposed strategy for HE4 detection in practical samples.

Reference:

S1. H. Zheng, H. Yi, H. Dai, D. Fang, Z. Hong, D. Lin, X. Zheng and Y. Lin, *Sensors and Actuators B: Chemical*, 2018, **269**, 27-35.

S2. F. Wang, C. Yang, M. Duan, Y. Tang and J. Zhu, *Biosensors and Bioelectronics*, 2015, **74**, 1022-1028.

S3. X. Wang, H. Gao, H. Qi, Q. Gao and C. Zhang, *Analytical Chemistry*, 2018, **90**, 3013-3018.

S4. S. Xie, Y. Dong, Y. Yuan, Y. Chai and R. Yuan, *Anal Chem*, 2016, **88**, 5218-5224.

S5. C. Hu, S. Duo, T. Liu, W. Li and R. Zhang, *Materials Letters*, 2010, **64**, 2472-2474.

S6. X. Zhao, J. Wang, H. Chen, H. Xu, L. Bai, W. Wang, H. Yang, D. Wei and B. Yuan, *Sensors and Actuators B: Chemical*, 2019, **301**.

S7. Z. Zhang, J. Feng, P. Huang, S. Li and F.-Y. Wu, *Sensors and Actuators B: Chemical*, 2019, **298**.

S8. C. Ding, J. Liang, Z. Zhou, Y. Li, W. Peng, G. Zhang, F. Zhang and X. Fan, *Chemical Engineering Journal*, 2019, **378**, 122205.

S9. X. Wang, Z. Chen, K. Li, X. Wei, Z. Chen, J. M. Ruso, Z. Tang and Z. Liu, *Colloids and Surfaces A: Physicochemical and Engineering Aspects*, 2019, **560**, 298-305.

S10. K. Deng, X. Liu, C. Li and H. Huang, *Biosensors and Bioelectronics*, 2018, **117**, 168-174.

S11. A. Sahu, W. I. Choi, J. H. Lee and G. Tae, *Biomaterials*, 2013, **34**, 6239-6248.

S12. P. A. Rasheed, R. P. Pandey, K. Rasool and K. A. Mahmoud, *Sensors and Actuators B: Chemical*, 2018, **265**, 652-659.

S13. J. Zhu, E. Ha, G. Zhao, Y. Zhou, D. Huang, G. Yue, L. Hu, N. Sun, Y. Wang, L. Y. S. Lee, C. Xu, K.-Y. Wong, D. Astruc and P. Zhao, *Coordination Chemistry Reviews*, 2017, **352**, 306-327.

S14. Y. Zhang, L. Wang, N. Zhang and Z. Zhou, *RSC Advances*, 2018, **8**, 19895-19905.

S15. H. Dai, L. Gong, G. Xu, S. Zhang, S. Lu, Y. Jiang, Y. Lin, L. Guo and G. Chen, *Electrochimica Acta*, 2013, **111**, 57-63.

S16. F. Anson, *Anal. Chem.* , 1964, **36**, 932.

S17. S. Wang, X. Zhao, I. Khimji, R. Akbas, W. Qiu, D. Edwards, D. W. Cramer, B. Ye and U. Demirci, *Lab Chip*, 2011, **11**, 3411-3418.

S18. Y. Tan, M. Li, X. Ye, Z. Wang, Y. Wang and C. Li, *Sensors and Actuators B: Chemical*, 2018, **262**, 982-990.

S19. M. Ge, C. Wei, M. Xu, C. Fang, Y. Yuan, R. Gu and J. Yao, *Analytical Methods*, 2015, **7**, 6489-6495.

S20. J. Yuan, R. Duan, H. Yang, X. Luo, M. Xi, J. Yuan, R. Duan, H. Yang, X. Luo and M. Xi, *Int*

J Nanomedicine, 2012, **2012**, 2921-2928.

S21. Z. Qiao, H. Zhang, Y. Zhou and J. Zheng, *Analytical Chemistry*, 2019, **91**, 5125-5132.

S22. X. Han, H. Zhang and J. Zheng, *Analytical Chemistry*, 2019, **91**, 2224-2230.

S23. L. Fan, Y. Yan, B. Guo, M. Zhao, J. Li, X. Bian, H. Wu, W. Cheng and S. Ding, *Sensors and Actuators B: Chemical*, 2019, **296**.

S24. Z. Ran, H. Yang, Z. Li, K. Wang, J. Zhao, X. Ran, G. Du and L. Yang, *ACS Sustainable Chemistry & Engineering*, 2020, **8**, 10161-10172.

S25. L. Xiao, I. Streeter, G. G. Wildgoose and R. G. Compton, *Sens. Actuators, B,* **2008**, 133, 118–127.

S26. Y. Chen, X. Chen, Z. Lin, H. Dai, B. Qiu, J. Sun, L. Zhang and G. Chen, *Electrochem. Commun*., **2009**, 11, 1142–1145.